Spin Hall Angle of Rhodium and its Effects on Magnetic Damping of $Ni_{80}Fe_{20}$ in Rh/$Ni_{80}Fe_{20}$ Bilayer

Bipul K. Mahato[1†] R. Medwal[1], S. Baidya[2], D. Kumar[3], S. N. Piramanayagam[3], and R. S. Rawat[1]***

[1]Natural Sciences and Science Education, National Institute of Education, Nanyang Technological University, 1 Nanyang Walk, Singapore 637616.

[2]Department of Physics & Astronomy, Rutgers University, Piscataway, New Jersey 08854, USA

[3]School of Physical and Mathematical Sciences, Nanyang Technological University, 21 Nanyang Link, Singapore 637371

**Corresponding author (email: rajdeep.rawat@nie.edu.sg), *Co-corresponding author (bipul.kumar.mahato@gmail.com)

ABSTRACT

We report the investigation of the spin Hall angle (SHA) of Rhodium (Rh) and the effective magnetic damping constant of $Ni_{80}Fe_{20}$ in Rh (10 nm)/$Ni_{80}Fe_{20}$ (10 nm) bilayer system using Spin Torque Ferromagnetic Resonance (STFMR) spectroscopy and density functional theory based analysis. The filtered DC output voltages from Rh (10 nm)/$Ni_{80}Fe_{20}$ (10 nm) bilayer system at different input signal frequencies and powers for a complete 360° angle were measured. The average magnetic damping constant of $Ni_{80}Fe_{20}$ is found to be 0.017 and the angle-dependent study shows a 2-fold symmetry with the in-plane anisotropy field of 120 Oe. The SHA of Rh is found to be 0.2 %. The results agrees well with the calculations based on density functional theory where we found spin Hall conductivity (σ_{xy}^{spinz}) at the charge-neutral Fermi level (EF) is positive and it's magnitude is $\sim 423 \left(\frac{\hbar}{e}\right)$ $(\mathrm{S/cm})$.

Keywords: Spin Hall conductivity, Rhodium, STFMR, Waveguide, Magnetic damping, $Ni_{80}Fe_{20}$ bilayer.

Introduction :

A considerable research interest in the search of new spin Hall materials suitable for efficent spin-orbit torques (SOT)[1,2] is driven by applications in magnetization switching, and magnetization auto-oscilations for logic and memory devices[3,4,5] The conversion efficiency from the charge current to spin current is quantified by the figure of merit known as spin Hall angle (SHA)[6,7,8]. Recently, materials, particularly metals and alloys, with much larger SHAs have been observed which include Pt (5.7±1.4%)[9], Pd(0.56 ± 0.07%)[10], Ag(0.68±0.07%)[11], $Cu_{76}Ir_{24}$(6.29 ± 0.19%)[12], and Au (8.7 ± 2.5%)[13,14]. The SOTs induced by these materials are reported to be large enough to induce motion of magnetic domain walls[15], excite spin waves[16–18] and switch the direction of magnetization vector in a uniform thin magnetic layer[19]. Along with SOTs, magnetic anisotropy[20,21], configurational anisotropy[22], and Gilbert damping parameter[15,23,24] become important which determine the critical operational characteristics of spintronic devices such as the threshold write current[25,26], switching time[27], and transition jitters[28]. Although the exact origins of the SOT are not fully understood, reported theories explained them as a combination of intrinsic mechanisms and extrinsic spin-dependent scattering inside the bulk of the materials[29]. Typically, extrinsic mechanisms are likely to dominate over the intrinsic mechanisms because of innate bulk disorder or impurities in the thin films[30]. Rhodium(Rh)[31] is positioned very close to the elements, mentioned above which are extensively studied, in the periodic table but there are no reports of its SHA in the literature. In order to measure the SHA in Rh, we have used spin-torque ferromagnetic resonance (STFMR), which involves diffusion of spin current from heavy metal (HM) to adjacent FM layer that exerts significant spin torque on the magnetization vector of the ferromagnetic layer[32,33,34]. The increase in magnetic damping parameter of Ni80Fe20/Rh indicate the presence of spin relaxation in Rh. The lineshape analysis were employed and the SHA of Rh is obtained to be about 0.2 %. To understand the orgin of the obtained 0.2% SHA, the density functional theory (DFT) calcutaion were perfomed by constructing Wannier functions using Wannier90 package48. Our calculation shows the presence of positive charge-neutral Fermi level (EF) in the Rh supporting the observation of positive spin Hall angle of Rh and also suggest dominant intrinsic orgin of charge to spin conversion in Ni80Fe20/Rh.

Experimental Methods :

In order to make the devices for the STFMR measurements, we spun coat the photoresist (AZ MIR 701) at 3500 rpm for 1 minute starting at acceleration of 2000 rpm/sec on the cleaned 10 mm × 10 mm Si/SiO_2 substrate. After that we baked the samples at 90 ºC for 1 minute. The prepared sample was then placed inside a microwriter (Durham, UK) where it is exposed to ultraviolet light scanning through a loaded soft mask pattern. After that we developed the resist by placing it inside AZ 736 developer for 25 seconds with continuous mild stirring followed by post-bake at 110 ºC for 1 minute. The developed resist pattern was checked using an optical microscope. Then we placed the substrate with patterned resist subjected to stacked deposition of $Rh(t_1)/Ni_{80}Fe_{20}(t_2)$ where t_1 = 2,5,7,10 and 15 nm and t_2 =10 nm done at Ar gas pressures of 3 mTorr and 40 Watt electrical power. Finally, lift off of the resist was performed to obtained stripes of $Rh/Ni_{80}Fe_{20}$ bilayer with dimension of 60 µm x 20 µm. In the second photolithography step, a copper co-planar waveguide (CPW) of 300 nm thickness and 100 µm wide signal line and 200 µm wide ground lines with inter-line spacing of 30 µm was fabricated on top of the stripes so that the stripe bridges the central conducting line and ground line of the CPW[35]. The fabricated devices were then used for the magneto-transport measurements in STFMR set-up. We have completed the

measurements in one go before the oxygen diffusion happened at the interface. A schematic of the Rh/$Ni_{80}Fe_{20}$ bilayer is shown in Figure 1(a). The sketch of the waveguide is shown in Figure 1(b).

The STFMR measurement set up[33] is equiped with microwave signal generator (Agilent), Bias-T, Lock-in-amplifiers, 3D vector magnets, and a high frequency probe station with nonmagnetic ground-source-ground (G-S-G) probes (picoprobes, GGB Industries). Signals in the radio frequency range (10 MHz to 20 GHz) with different powers (varying from -5dB to 20 dB) are typically sent to the CPW, which is grounded at the other end. The back reflected signal is collected by the same probe. The AC component of the collected signal is then filtered out by a bias-T and the DC component is collected by the lock in amplifier. The collected DC component of the signal is plotted with the external magnetic field. Then, symmetric and asymmetric Lorentz function is fitted with the signal to obtain different parameters such as resonance frequency, resonance line width, amplitude of the symmetric and asymmetric components. In this work, the STFMR spectra were recorded by sweeping the magnetic field (H= -1 kOe to 1 kOe) measurements for constant frequency. The measurements were also perfomed as a function of in-plane magnetic field angle ϕ (0º to 360º at step of 10º). The geometric configuration of the applied field is shown in the Figure 1(a).

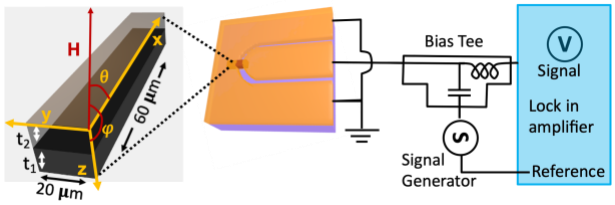

Figure 1. (a) The design of Rh(t_1)/$Ni_{80}Fe_{20}$(t_2) bilayer of size 60 µm x 20 µm on SiO_2 fabricated using photolithography. The applied magnetic field (H) direction (θ, φ) with respect to the length of the bilayer bar is shown inset. (b) 300 nm thick copper co-planner waveguide is made on top of the bilayer bar. (c) The microwave signal from the signal generator is sent to the device through GSG probes and the returned DC signal is collected to the lock in amplifiers after filtering out the AC component by a bias-T.

Results and discussions :

First, the STFMR spectra of a $Ni_{80}Fe_{20}$ strip of size 30 µm × 10 µm and 10 nm thickness was measured at increasing and decreasing bias fields at $\phi = 45^o$ to observe the anisotropic magnetoresistance (AMR) behaviour in $Ni_{80}Fe_{20}$ stripe. Subsequently, the Rh(t_1)/$Ni_{80}Fe_{20}$(t_2) bilayer samples were measured with field sweep at input frequencies and powers of 3, 4, 5, 6, 7 GHz and 16 dB, respectively. The DC signal amplitude increases proportionally with the input power which indicates the induced precession is in the small angle regime (presented in the supplementary material). In general, such magnetization dynamics are described by the following equation[35]

$$\frac{d\hat{m}}{dt} = \gamma \hat{m} \times \vec{H}_{eff} + \alpha \hat{m} \times \frac{d\hat{m}}{dt} + \frac{h}{4\pi e \mu_0 M_s t} J_{s,rf}(\hat{m} \times \hat{\sigma} \times \hat{m}) - \gamma(\hat{m} \times \vec{H}_{rf}) \quad (1)$$

Where γ is the free electron gyromagnetic ratio, $\hat{m}, \hat{\sigma}$, are unit vector of magnetization, electrical connductivity, respectively and $J_{s,rf}$ and H_{rf} represents the oscillating spin current density injected into Py and the Oersted field generated by the rf current. Whereas the acquired mixed signal can be fitted with the following equations[35,36,37]

$$V_{mix} = -\frac{1}{4}\frac{dR}{d\theta}\frac{\gamma I_{rf} cos\theta}{\beta 2\pi (df/dH)_{H_{ext}=H_0}}[SF_S(H_{ext}) + AF_A(H_{ext})] \quad (2)$$

where,

$$F_S(H_{ext}) = \frac{\beta^2}{[\beta^2+(H_{ext}-H_0)^2]},$$

$$F_A(H_{ext}) = \frac{\beta(H_{ext}-H_0)}{[\beta^2+(H_{ext}-H_0)^2]},$$

$$S = \frac{\hbar J_{S,rf}}{2e\mu_0 M_s t} \text{ and } A = H_{rf}\left[1+\frac{4\pi M_{eff}}{H_{ext}}\right]^{1/2} \qquad (3)$$

Where β represents the linewidth of the signal.

The obtained resonance linewidths are used for the calculation of effective damping constant (α_{eff}) of $Ni_{80}Fe_{20}$ and $Ni_{80}Fe_{20}$ interfacing Rh layer. The STFMR spectra for Rh/$Ni_{80}Fe_{20}$ bilayer stripes with different thicknesses of Rh and $Ni_{80}Fe_{20}$ layers were measured and the corresponding plots are shown in Figure 2(a).

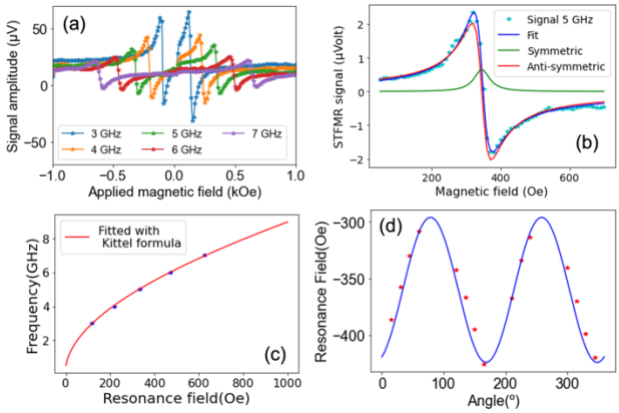

Figure 2 (a) The STFMR signal from the Rh(10)/$Ni_{80}Fe_{20}$(10) bilayer at 3, 4, 5, 6 and 7 GHz frequencies are shown. (b) The ferromagnetic resonance (FMR) fields, linewidths and signal amplitudes were extracted by fitting the Lorentzian functions and the symmetric and asymmetric components of the fitting function are plotted, together. (c) The dependence of FMR field on applied frequencies is shown which follows Kittel equation. The magnetic parameters of $Ni_{80}Fe_{20}$ has been extracted from the fitting. (d) Angular variation of applied magnetic field reflects two-fold shape anisotropy of the rectangular $Ni_{80}Fe_{20}$ stripe. The anisotropy field of Rh/$Ni_{80}Fe_{20}$ stripe has been found to be 120 Oe.

A typical fitting of Lorentz function on the signal spectrum has been done and the symmetric and asymmetric components of the fitting curve are plotted together in Figure 2(b). Resonance field as a function of the RF excitation frequency was fitted with Kittel's formula (refer to equation 4)[38] and shown in Figure 2(c), and material parameters such as saturation magnetization, and anisotropy field are extracted.

$$f = \frac{\gamma}{2\pi}\sqrt{(H+H_{K_{eff}})(H+H_{K_{eff}}+4\pi M_s)} \qquad (4)$$

From the fitting, we obtain saturation magnetization M_s= 760 emu/cc and effective anisotropy field $H_{K_{eff}}$= 3.8 Oe for Rh(10)/$Ni_{80}Fe_{20}$(10) bilayer. Values of $H_{K_{eff}}$ are extracted for different thicknesses of the Rh layers, which show an increment with decreament of t_1 and can be seen in the supplementary information. The extracted resonance fields were fitted with $A\,cos(2\theta)$ that helped us to obtain the value of A as 120 Oe which is shown in Figure 2(d). This indicates a 2-fold configurational anisotropy because of the geometrical shape of the $Ni_{80}Fe_{20}$ sample.

Increase in M_s were observed as reflected by changes in $H_{K_{eff}}$ as we varied the Rh thickness[20–22]. In most of the cases, $H_{K_{eff}}$ is negative and increases as t_1 decreases to a maximum value of -35 Oe. We have done a linear fittting on the frequency versus extracted linewidths data for samples with varying Rh thicknesses. We have calculated damping parameter of Rh using the following relation[39],

$$\Delta H = \Delta H_0 + 1.16 \times \frac{2\pi f}{\gamma}\alpha_{eff} \qquad (5)$$

where ΔH_0 is the y-axis intercept of frequency vs linewidth curve, in Figure 3(a). In this case ΔH_0=0.48 Oe. $\gamma = 1.76 \times 10^{11} \frac{rad}{s.T}$ is the gyromagnetic ratio of free electron. The change in value of ΔH_0 and slope of the lines in Figure 3(a) indicate the change in homogeneity of magnetization within the sample caused by interface roughness whiich depends on the Rh layer thicknesses[24,40–42]. The measured signnals for Rh layer thicknesses of 1 nm, 2 nm, 7 nm and 15 nm are shown in the supplementary file. We have calculated α_{eff} at different frequencies for different thicknesses of Rh and plotted and averaged out in Figure 3(b).

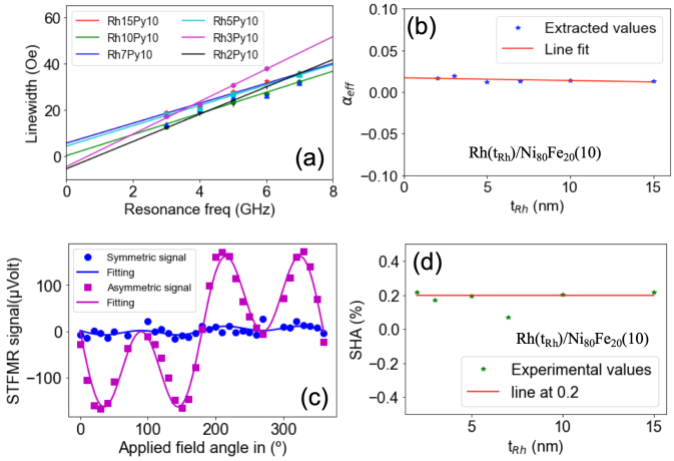

Figure 3 (a) The signal linewidths at varying frequencies for different thicknesses of Rh are fitted with a straight line which intercepts the y-axis at 0.48 Oe. (b) The effective damping constant α_{eff} for Rh(t_1)/Ni$_{80}$Fe$_{20}$(10) where t_1= 2, 5, 7, 10 and 15 nm are plotted against t_1 and a straight line is drawn to guide the eyes. (c) The amplitudes of the symmetric and asymmmtric signals are plotted against all different applied field angles which follows the $Acos\theta sin2\theta$ curve as shown. (d) Extracted SHA has been plotted for different Rh thicknesses.

The averaged α_{eff} has been found to be 0.017 which is higher than the damping factor of pure permalloy (0.008)[43] and less than the value (0.025) obtained by doping (20 atomic percentage) of Rh into Ni$_{80}$Fe$_{20}$ [44]. This nullify the effect of unwanted doping. The higher value of α_{eff} can be due to the spin pumping effect[45,46] caused by strong SOC of HM and orbital hybridization with the 3d orbitals in the transition metal FM[47,48,49].

The angle dependence nature of the symmetric and assymmetric component of the mixed signal are fitted with cosθsin2θ function and shown in Figure 3(c). For the calculation of spin Hall angle, the values of the symmetric (S) and asymmetric (A) components are extracted which are found to be maximum at applied field direction at multiples of 45° to the stripe length. The symmetric component is proportional to the damping like torque and asymmetric component corresponds to the sum of the Oersted field and field-like effective torques.[35,50] The SHA is calculated by taking the ratio of amplitudes of symmetric and asymmetric components of the Lorentz fitting at 45°. We expect symmetric Lorentzian peak to be proportional to $J_{S,rf}$ and an asymmetric peak proportional to H_{rf}. Thus, the following equation is used to calculate the SHA of Rh[35],

$$\theta_{SH} = \frac{J_{S,rf}}{J_{C,rf}} = \frac{S}{A}\frac{e\mu_0 M_s t d}{\hbar}\left[1 + \frac{4\pi M_{eff}}{H_{ext}}\right]^{1/2} \qquad (6)$$

M_{eff} is calculated from the sum of $H_{K_{eff}}$ and $4\pi M_s$. The SHA calculated for $Rh(t_1)/Ni_{80}Fe_{20}(10)$ at t_1 varying from 2 nm to 15 nm are plotted in Figure 3(d) and a line drawn at the maximum value of SHA of 0.2% as a guide to the eyes. Rhodium shows a positive SHA in our study similar to the theoretical report.[51]

Experimentally observed spin Hall effect (SHE) may arise from either intrinsic contribution or extrinsic contribution. Therefore, we have studied the electronic density of states (DOS) and spin Hall conductivity (SHC)[52] using first-principle density functional theory (DFT) and Wannier90 based tight-binding model. In the Figure 4(a), the nonmagnetic electronic DOS without spin-orbit coupling shows that the Fermi level is dominated by Rh d orbital with a nonmagnetic ground state. The Rh s orbital is totally empty and placed at ~15 eV with respect to the Fermi level. The electronic band structure plotted along the high-

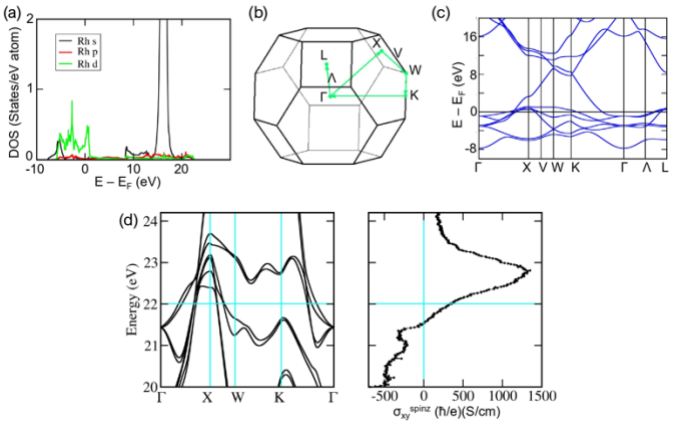

Figure 4 (a) PBE+SOC DOS with various orbital contributions from Rh atom. (b) The BZ of the bulk Rh with high-symmetry direction in green line. (c) The PBE+SOC electronic band structure plotted along the high-symmetry direction. (d) The Variation of SHC (σ_{xy}^{spinz}) with Fermi level position.

symmetry direction (shown in Figure 4(b) with the BZ) with spin-orbit coupling shows highly entangled bands (Figure 4(c)) crossing Fermi level. A few band Hamiltonian is obtained from all band Hamiltonian corresponding to the ground state as calculated using DFT, by constructing Wannier functions using Wannier90 package[53]. From the real space low energy Hamiltonian, obtained from Wannier90, a spin Berry curvature (SBC) like function was calculated as implemented in the Wannier90 package. Then the SBC is integrated over entire Brillouin Zone to calculate the SHC σ_{xy}^{spinz} by summing over occupied bands. The variation of SHC with Fermi level position is plotted in the Figure 4(d). It is evident that the σ_{xy}^{spinz} at the charge-neutral Fermi level (EF) is positive and the magnitude is $\sim 423 \left(\frac{\hbar}{e}\right)$ (S/cm). The equivalent spin Hall angle caluclated using the following formula[54]

$$\theta_{SH} = \frac{\sigma_{xy}^{spinz} e}{\sigma_{xx}^{c} \hbar} \qquad (7),$$

where σ_{xx}^{c} is electtrical conducttivity of Rh = 2.0 x 10^5 S/cm measured from a Rh film deposited at the same condition. We obtained $\theta_{SH} = 0.211$ % which is very close to the experimentally measured value of spin Hall angle .

Conclusion :

In summary, the spin-torque ferromagnetic resonance measurements on stripes of $Rh(t_1)/Ni_{80}Fe_{20}(10)$ bilayers have been performed. We have found that the effective Gilbert damping constant of $Ni_{80}Fe_{20}$ is 0.017, The resonance field shows 2-fold symmetry with 120 Oe anisotropy field due to the shape anisotropy of the rectangular stripes. Experimetally obtained SHA of Rh is 0.2 % and spin conductivity calculated using DFT proves it's origin as intrisic. The findings will pave the way in material selection for future research on spin orbit torque based spintronics applications.

Data Availibity Statement

Data can be availed from the corresponding author on request.

Present Address

†School of Physical Sciences, Indian Association for the Cultivation of Science, 2A and 2B, Raja S C Mullick Road, Jadavpur, Kolkata 700032, India.

Author Contributions :

BKM prepared the samples and performed the measurements, analysis in consultation with RSR, RM DK and SNP. SB performed the DFT calculation. All authors wrote the manuscript jointly.

The authors declare that they have no conflict of interest.

Acknowledgements

We acknowledge the financial support from Ministry of Education (MOE), Singapore through grant number MOE2019-T2-1-058 and also the National Research Foundation (NRF), Singapore for grant NRF-CRP21-2018-0003.

References.

(1) Jover-galtier, J. A.; Anado, A.; Manuel, J.; Olleros-rodr, P.; Miranda, R.; Camarero, J.; Perna, P. Spin-Orbit Torque from the Introduction of Cu Interlayers in Pt / Cu / Co / Pt Nanolayered Structures for Spintronic Devices. *ACS Appl. Nano Mater.* **2021**, *4*, 487–492. https://doi.org/10.1021/acsanm.0c02808.

(2) Seki, T.; Lau, Y.; Iihama, S.; Takanashi, K. PHYSICAL REVIEW B 104 , 094430 (2021) Spin-Orbit Torque in a Ni-Fe Single Layer. *Phys. Rev. B* **2021**, *104* (9), 94430. https://doi.org/10.1103/PhysRevB.104.094430.

(3) Demidov, V. E.; Urazhdin, S.; de Loubens, G.; Klein, O.; Cros, V.; Anane, A.; Demokritov, S. O. Magnetization Oscillations and Waves Driven by Pure Spin Currents. *Phys. Rep.* **2017**, *673*, 1–31. https://doi.org/10.1016/j.physrep.2017.01.001.

(4) Urazhdin, S.; Demidov, V. E.; Ulrichs, H.; Kendziorczyk, T.; Kuhn, T.; Leuthold, J.; Wilde, G.; Demokritov, S. O. Nanomagnonic Devices Based on the Spin-Transfer Torque. *Nat. Nanotechnol.* **2014**, *9* (7), 509–513. https://doi.org/10.1038/nnano.2014.88.

(5) Ciccarelli, C.; Hals, K. M. D.; Irvine, A.; Novak, V.; Tserkovnyak, Y.; Kurebayashi, H.; Brataas, A.; Ferguson, A. Magnonic Charge Pumping via Spin-Orbit Coupling. *Nat. Nanotechnol.* **2015**, *10* (1), 50–54. https://doi.org/10.1038/nnano.2014.252.

(6) Murakami, S.; Nagaosa, N. Spin Hall Effect. *Compr. Semicond. Sci. Technol.* **2011**, *1–6*, 222–278. https://doi.org/10.1016/B978-0-44-453153-7.00061-4.

(7) Idrish Miah, M. Direct Detection of Electron Spins and Doping Effects in Spin-Polarized Electron Transport in Gallium Arsenide. *J. Mater. Sci.* **2010**, *45* (1), 124–129. https://doi.org/10.1007/s10853-009-3901-1.

(8) Huong, P. T.; Muoi, D.; Phuc, H. V.; Nguyen, C. V.; Hoa, L. T.; Hoi, B. D.; Hieu, N. N. Low-Energy Bands, Optical Properties, and Spin/Valley-Hall Conductivity of Silicene and Germanene. *J. Mater. Sci.* **2020**, *55* (30), 14848–14857. https://doi.org/10.1007/s10853-020-05044-0.

(9) Keller, S.; Mihalceanu, L.; Schweizer, M. R.; Lang, P.; Heinz, B.; Geilen, M.; Brächer, T.; Pirro, P.; Meyer, T.; Conca, A.; Karfaridis, D.; Vourlias, G.; Kehagias, T.; Hillebrands, B.; Papaioannou, E. T. Determination of the Spin Hall Angle in Single-Crystalline Pt Films from Spin Pumping Experiments. *New J. Phys.* **2018**, *20* (5). https://doi.org/10.1088/1367-2630/aabc46.

(10) Tao, X. D.; Feng, Z.; Miao, B. F.; Sun, L.; You, B.; Wu, D.; Du, J.; Zhang, W.; Ding, H. F. The Spin Hall Angle and Spin Diffusion Length of Pd Measured by Spin Pumping and Microwave Photoresistance. *J. Appl. Phys.* **2014**, *115* (17), 2012–2015. https://doi.org/10.1063/1.4862215.

(11) Santos, O. A.; Silva, E. F.; Gamino, M.; Mendes, J. B. S.; Rezende, S. M.; Azevedo, A. Investigation of Large Enhancement of Spin Hall Angle in Heterostructures of Ag Nanoparticles Randomly Grown in Pt. *AIP Adv.* **2019**, *9* (3), 1–5. https://doi.org/10.1063/1.5079813.

(12) Masuda, H.; Modak, R.; Seki, T.; Uchida, K.; Lau, Y.-C.; Sakuraba, Y.; Iguchi, R.; Takanashi, K. Large Spin-Hall Effect in Non-Equilibrium Binary Copper Alloys beyond the Solubility Limit. *Commun. Mater.* **2020**, *1* (1). https://doi.org/10.1038/s43246-020-00076-0.

(13) Isasa, M.; Villamor, E.; Hueso, L. E.; Gradhand, M.; Casanova, F. Temperature Dependence of Spin Diffusion Length and Spin Hall Angle in Au and Pt. *Phys. Rev. B - Condens. Matter Mater. Phys.* **2015**, *91* (2), 1–7. https://doi.org/10.1103/PhysRevB.91.024402.

(14) Brangham, J. T.; Meng, K. Y.; Yang, A. S.; Gallagher, J. C.; Esser, B. D.; White, S. P.; Yu, S.; McComb, D. W.; Hammel, P. C.; Yang, F. Thickness Dependence of Spin Hall Angle of Au Grown on Y3 F E5 O12 Epitaxial Films. *Phys. Rev. B* **2016**, *94* (5), 6–11. https://doi.org/10.1103/PhysRevB.94.054418.

(15) Mizukami, S.; Ando, Y.; Miyazaki, T. Effect of Spin Diffusion on Gilbert Damping for a Very Thin

Permalloy Layer in Cu/Permalloy/Cu/Pt Films. *Phys. Rev. B - Condens. Matter Mater. Phys.* **2002**, *66* (10), 1044131–1044139. https://doi.org/10.1103/PhysRevB.66.104413.

(16) Mahato, B. K.; Rana, B.; Kumar, D.; Barman, S.; Sugimoto, S.; Otani, Y.; Barman, A. Tunable Spin Wave Dynamics in Two-Dimensional Ni 80 Fe 20 Nanodot Lattices by Varying Dot Shape. **2014**. https://doi.org/10.1063/1.4890088.

(17) Jaris, M.; Yahagi, Y.; Mahato, B. K.; Dhuey, S.; Cabrini, S.; Nikitin, V.; Stout, J.; Hawkins, A. R.; Schmidt, H. Intrinsic Spin Dynamics in Optically Excited Nanoscale Magnetic Tunnel Junction Arrays Restored by Dielectric Coating. *Appl. Phys. Lett.* **2016**, *109* (20). https://doi.org/10.1063/1.4967848.

(18) Allwood, D. A.; Xiong, G.; Faulkner, C. C.; Atkinson, D.; Petit, D.; Cowburn, R. P. Magnetic Domain-Wall Logic. *Science (80-.).* **2005**, *309* (5741), 1688–1692. https://doi.org/10.1126/science.1108813.

(19) Liu, L.; Pai, C. F.; Li, Y.; Tseng, H. W.; Ralph, D. C.; Buhrman, R. A. Spin-Torque Switching with the Giant Spin Hall Effect of Tantalum. *Science (80-.).* **2012**, *336* (6081), 555–558. https://doi.org/10.1126/science.1218197.

(20) Johnson, M. J.; Bloemen, P. J. H.; Broeder, F. J. A. den; Vries, J. J. de. Reports on Progress in Physics Related Content Magnetic Anisotropy in Metallic Multilayers. *Reports Prog. Phys.* **1996**, *59* (11), 1409–1458.

(21) Deka, A.; Rana, B.; Anami, R.; Miura, K.; Takahashi, H.; Otani, Y. C.; Fukuma, Y. Electric-Field Control of Interfacial in-Plane Magnetic Anisotropy in CoFeB/MgO Junctions. *Phys. Rev. B* **2020**, *101* (17), 1–8. https://doi.org/10.1103/PhysRevB.101.174405.

(22) Mahato, B. K.; Choudhury, S.; Mandal, R.; Barman, S.; Otani, Y.; Barman, A. Tunable Configurational Anisotropy in Collective Magnetization Dynamics of Ni<inf>80</Inf>Fe<inf>20</Inf> Nanodot Arrays with Varying Dot Shapes. *J. Appl. Phys.* **2015**, *117* (21). https://doi.org/10.1063/1.4921976.

(23) Gerrits, T.; Schneider, M. L.; Silva, T. J. Enhanced Ferromagnetic Damping in Permalloy/Cu Bilayers. *J.*

Appl. Phys. **2006**, *99* (2). https://doi.org/10.1063/1.2159076.

(24) Rantschler, J. O.; Maranville, B. B.; Mallett, J. J.; Chen, P.; McMichael, R. D.; Egelhoff, W. F. Damping at Normal Metal/Permalloy Interfaces. *IEEE Trans. Magn.* **2005**, *41* (10), 3523–3525. https://doi.org/10.1109/TMAG.2005.854956.

(25) Sun, J. Z. Spin-Current Interaction with a Monodomain Magnetic Body: A Model Study. *Phys. Rev. B - Condens. Matter Mater. Phys.* **2000**, *62* (1), 570–578. https://doi.org/10.1103/physrevb.62.570.

(26) Visscher, P. B.; Apalkov, D. M. Fokker-Planck Calculation of Spin-Torque Resistance Hysteresis and Switching Currents. *J. Appl. Phys.* **2005**, *97* (10), 10–13. https://doi.org/10.1063/1.1850813.

(27) Wang, X.; Gao, K.; Zhou, H.; Itagi, A.; Seigler, M.; Gage, E. HAMR Recording Limitations and Extendibility. *IEEE Trans. Magn.* **2013**, *49* (2), 686–692. https://doi.org/10.1109/TMAG.2012.2221689.

(28) Huang, P. W.; Victora, R. H. Heat Assisted Magnetic Recording: Grain Size Dependency, Enhanced Damping, and a Simulation/Experiment Comparison. *J. Appl. Phys.* **2014**, *115* (17), 5–7. https://doi.org/10.1063/1.4862719.

(29) Mahfouzi, F.; Mishra, R.; Chang, P. H.; Yang, H.; Kioussis, N. Microscopic Origin of Spin-Orbit Torque in Ferromagnetic Heterostructures: A First-Principles Approach. *Phys. Rev. B* **2020**, *101* (6), 1–6. https://doi.org/10.1103/PhysRevB.101.060405.

(30) Ramaswamy, R.; Qiu, X.; Dutta, T.; Pollard, S. D.; Yang, H. Hf Thickness Dependence of Spin-Orbit Torques in Hf/CoFeB/MgO Heterostructures. *Appl. Phys. Lett.* **2016**, *108* (20), 1–6. https://doi.org/10.1063/1.4951674.

(31) Duan, H.; Yan, N.; Yu, R.; Chang, C.; Zhou, G.; Hu, H.; Rong, H.; Niu, Z.; Mao, J.; Asakura, H.; Tanaka, T.; Dyson, P. J.; Li, J.; Li, Y. Ultrathin Rhodium Nanosheets. *Nat Commun* **2014**, *5* (3093), 1–8. https://doi.org/10.1038/ncomms4093.

(32) Wang, T.; Wang, W.; Xie, Y.; Warsi, M. A.; Wu, J.; Chen, Y.; Lorenz, V. O.; Fan, X.; Xiao, J. Q. Large Spin Hall Angle in Vanadium Film/639/766/119/1001/639/766/119/544/120/123/142/126/144/145 Article. *Sci. Rep.* **2017**, *7* (1), 1–6. https://doi.org/10.1038/s41598-017-01112-9.

(33) Medwal, R.; Gupta, S.; Rawat, R. S.; Subramanian, A.; Fukuma, Y. Spin Pumping in Asymmetric Fe50Pt50/Cu/Fe20Ni80 Trilayer Structure. *Phys. Status Solidi - Rapid Res. Lett.* **2019**, *13* (10), 1–6. https://doi.org/10.1002/pssr.201900267.

(34) Alotibi, S.; Hickey, B. J.; Teobaldi, G.; Ali, M.; Barker, J.; Poli, E.; Regan, D. D. O.; Ramasse, Q.; Burnell, G.; Patchett, J.; Ciccarelli, C.; Alyami, M.; Moorsom, T.; Cespedes, O. Enhanced Spin–Orbit Coupling in Heavy Metals via Molecular Coupling. *ACS Appl. Mater. Interfaces* **2021**, *13*, 5228−5234. https://doi.org/10.1021/acsami.0c19403.

(35) Liu, L.; Moriyama, T.; Ralph, D. C.; Buhrman, R. A. Spin-Torque Ferromagnetic Resonance Induced by the Spin Hall Effect. *Phys. Rev. Lett.* **2011**, *106* (3), 1–4. https://doi.org/10.1103/PhysRevLett.106.036601.

(36) Gupta, S.; Medwal, R.; Kodama, D.; Kondou, K.; Otani, Y. C.; Fukuma, Y. Important Role of Magnetization Precession Angle Measurement in Inverse Spin Hall Effect Induced by Spin Pumping. *Appl. Phys. Lett.* **2017**, *110* (2). https://doi.org/10.1063/1.4973704.

(37) Shashank, U.; Medwal, R.; Shibata, T.; Nongjai, R.; Vas, J. V.; Duchamp, M.; Asokan, K.; Rawat, R. S.; Asada, H.; Gupta, S.; Fukuma, Y. Enhanced Spin Hall Effect in S-Implanted Pt. *Adv. Quantum Technol.* **2021**, *4* (1), 1–6. https://doi.org/10.1002/qute.202000112.

(38) Kittel, C. On the Theory of Ferromagnetic Resonance Absorption. *Phys. Rev.* **1948**, *73* (2), 155–161. https://doi.org/10.1103/PhysRev.73.155.

(39) Kuanr, B. K.; Camley, R. E.; Celinski, Z. Extrinsic Contribution to Gilbert Damping in Sputtered NiFe Films by Ferromagnetic Resonance. *J. Magn. Magn. Mater.* **2005**, *286* (SPEC. ISS.), 276–281.

https://doi.org/10.1016/j.jmmm.2004.09.080.

(40) Akomolafe, T.; Johnson, G. W. The Effect of Sheet Thickness on the Magnetic Properties of 77 Wt% Ni Permalloys. *J. Mater. Sci.* **1989**, *24* (1), 349–354. https://doi.org/10.1007/BF00660979.

(41) Hu, C. X.; Wu, Y. S.; Wei, H. Y.; Shi, Y. C.; Wu, L. L. A Comparative Study of the Effects of Cu, Rh Doping on the Microstructure, Morphological and Optical Properties of Tin Dioxide Nanocrystallines. *J. Mater. Sci.* **2005**, *40* (23), 6301–6306. https://doi.org/10.1007/s10853-005-3139-5.

(42) Katida, M.; Shimizu, N.; Tanabe, H. Reactions between Zirconium / Permalloy Bilayer Thin Films. *J Mater. Sci.* **1991**, *26*, 835–838.

(43) Mizukami, S.; Abe, H.; Watanabe, D.; Oogane, M.; Ando, Y.; Miyazaki, T. Gilbert Damping for Various Ni80Fe20 Thin Films Investigated Using All-Optical Pump-Probe Detection and Ferromagnetic Resonance. *Appl. Phys. Express* **2008**, *1* (12), 1213011–1213013. https://doi.org/10.1143/APEX.1.121301.

(44) Rantschler, J. O.; Mcmichael, R. D.; Castillo, A.; Shapiro, A. J.; Jr, W. F. E.; Maranville, B. B.; Pulugurtha, D.; Chen, A. P.; Connors, L. M. Effect of 3 d , 4 d , and 5 d Transition Metal Doping on Damping in Permalloy Thin Films Effect of 3 d , 4 d , and 5 d Transition Metal Doping on Damping in Permalloy. *J. Appl. Phys.* **2007**, *101* (033911), 1–5. https://doi.org/10.1063/1.2436471.

(45) Wei, J.; He, C.; Wang, X.; Xu, H.; Liu, Y.; Guang, Y.; Wan, C.; Feng, J.; Yu, G.; Han, X. Characterization of Spin-Orbit Torque Efficiency in Magnetic Heterostructures with Perpendicular Magnetic Anisotropy via Spin-Torque Ferromagnetic Resonance. *Phys. Rev. Appl.* **2020**, *13* (3), 1. https://doi.org/10.1103/PhysRevApplied.13.034041.

(46) Ou, Y.; Pai, C. F.; Shi, S.; Ralph, D. C.; Buhrman, R. A. Origin of Fieldlike Spin-Orbit Torques in Heavy Metal/Ferromagnet/Oxide Thin Film Heterostructures. *Phys. Rev. B* **2016**, *94* (14), 1–6. https://doi.org/10.1103/PhysRevB.94.140414.

(47) Sandler, G. M.; Bertram, H. N.; Silva, T. J.; Crawford, T. M. Determination of the Magnetic Damping Constant in NiFe Films. *J. Appl. Phys.* **1999**, *85* (8 II A), 5080–5082. https://doi.org/10.1063/1.370096.

(48) C. Swindells, H. Głowinski, Y. Choi, D. Haskel, P. P. Michałowski, T. Hase, P. Kuswik, Atkinson, and D. Proximity-Induced Magnetism and the Enhancement of Damping in Ferromagnetic / Heavy Metal Systems. *Appl. Phys. Lett.* **2021**, *152401* (October). https://doi.org/10.1063/5.0064336.

(49) Zilu Wang, Houyi Cheng, Kewen Shi, Yang Liu, Junfeng Qiao, Daoqian Zhu, W. C.; Xueying Zhang, Sylvain Eimer, Dapeng Zhu, Jie Zhang, Albert Fert, and W. Z. Nanoscale. *Nanoscale* **2020**. https://doi.org/10.1039/D0NR02762F.

(50) Xu, Z.; Dao, G.; Wong, H.; Tang, J.; Liu, E.; Gan, W.; Xu, F.; Lew, W. S. Giant Spin Hall E Ff Ect in Cu − Tb Alloy Thin Films. *ACS Appl. Mater. Interfaces* **2020**, *12*, 32898−32904. https://doi.org/10.1021/acsami.0c07441.

(51) Tanaka, T.; Kontani, H.; Naito, M.; Naito, T.; Hirashima, D. S.; Yamada, K.; Inoue, J. Intrinsic Spin Hall Effect and Orbital Hall Effect in 4d and 5d Transition Metals. *Phys. Rev. B - Condens. Matter Mater. Phys.* **2008**, *77* (16), 1–16. https://doi.org/10.1103/PhysRevB.77.165117.

(52) Parfenov, O. E.; Averyanov, D. V; Tokmachev, A. M.; Karateev, I. A.; Taldenkov, A. N.; Kondratev, O. A.; Storchak, V. G. Interface-Induced Anomalous Hall Conductivity in a Con Fi Ned Metal. *ACS Appl. Mater. Interfaces* **2018**, *10*, 35589–35598. https://doi.org/10.1021/acsami.8b10962.

(53) Pizzi et al, G. Wannier90 as a Community Code: New Features and Applications. *J. Phys. Condens. Matter* **2020**, *32* (16), 165902. https://doi.org/10.1088/1361-648x/ab51ff.

(54) Hoffmann, A. Spin Hall Effects in Metals. *IEEE Trans. Magn.* **2013**, *49* (10). https://doi.org/10.1109/TMAG.2013.2262947.